ACS OMEGA

http://pubs.acs.org/journal/acsodf

Article

α-Glucosidase and PTP-1B Inhibitors from *Malbranchea dendritica*

Daniela Rebollar-Ramos, Berenice Ovalle-Magallanes, Juan Francisco Palacios-Espinosa, Martha Lydia Macías-Rubalcava, Huzefa A. Raja, Martín González-Andrade, and Rachel Mata*

Cite This: *ACS Omega* 2021, 6, 22969−22981

Read Online

ACCESS | Metrics & More | Article Recommendations | Supporting Information

ABSTRACT: An extract from a PDB static culture of *Malbranchea dendritica* exhibited α-glucosidase and PTP-1B inhibitory activities. Fractionation of the active extract led to the isolation of gymnoascolide A (**1**), a γ-butenolide, and xanthones sydowinin A (**2**), sydowinin B (**3**), and AGI-B4 (**4**), as well as orcinol (**5**). Compound **1** exhibited important inhibitory activity against yeast α-glucosidase (IC_{50} = 0.556 ± 0.009 mM) in comparison to acarbose (IC_{50} = 0.403 ± 0.010 mM). Kinetic analysis revealed that **1** is a mixed-type inhibitor. Furthermore, compound **1** significantly reduced the postprandial peak in mice during a sucrose tolerance test at the doses of 5.16 and 10 mg/kg. Compound **1** was reduced with Pd/C to yield a mixture of enantiomers **1a** and **1b**; the mixture showed similar activity against α-glucosidase (IC_{50} = 0.396 ± 0.003 mM) and kinetic behavior as the parent compound but might possess better drug-likeness properties according to SwissADME and Osiris Property Explorer tools. Docking analysis with yeast α-glucosidase (pdb: 3A4A) and the C-terminal subunit of human maltase-glucoamylase (pdb: 3TOP) predicted that **1**, **1a**, and **1b** bind to an allosteric site of the enzymes. Compounds **1**−**5** were evaluated against PTP-1B, but only xanthone **3** moderately inhibited in a noncompetitive fashion the enzyme with an IC_{50} of 0.081 ± 0.004 mM. This result was consistent with that of docking analysis, which revealed that **3** might bind to an allosteric site of the enzyme. From the inactive barley-based semisolid culture of *M. dendritica*, the natural pigment erythroglaucin (**6**) and the nucleosides deoxyadenosine (**7**), adenosine (**8**), thymidine (**9**), and uridine (**10**) were also isolated and identified.

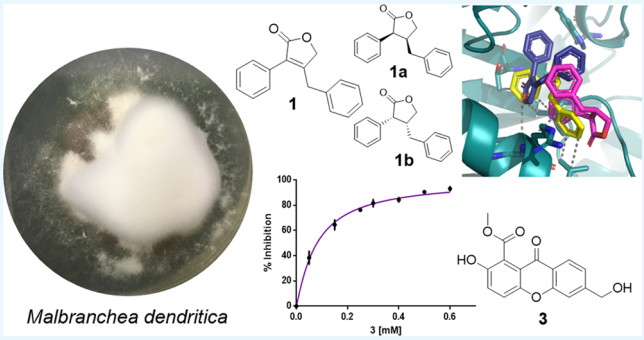

INTRODUCTION

In 2019, the International Diabetes Federation (IDF) estimated that more than 450 million people suffered from type 2 diabetes mellitus (T2DM), causing more than 4.2 million deaths that year.[1] Thus, T2DM represents a significant global health problem with a significant negative economic impact.

The treatment of T2DM includes a healthy lifestyle and the use of various drugs and insulin.[2] Nevertheless, there is a need for new, more efficient therapies targeting different or known proteins involved in glucose absorption or signaling cascades implicated in this complex disease. Protein tyrosine phosphatase 1B (PTP-1B), a negative modulator of insulin and leptin signaling, is a highly validated pharmacological target against insulin resistance and obesity.[3] PTP-1B plays a critical role in the control of glucose and energy homeostasis. Thus, many research programs are looking for new selective inhibitors of PTP-1B. Regarding α-glucosidases (AGs), these enzymes hydrolyze larger carbohydrate molecules to glucose; their inhibition can delay the liberation of glucose from dietary carbohydrates, retarding glucose absorption and lowering the postprandial blood glucose peak. In combination with first-choice drugs, AGs reduced the incidence of cardiovascular complications.[4]

Based on the above considerations, we have established a systematic program to discover new AG and PTP-1B inhibitors from fungi of the genus *Malbranchea*. Thus, *Malbranchea flavorosea* Sigler & Carmichael yielded a few polyketides and dipeptides with AG inhibitory activity, *in vitro* and *in vivo*.[5,6] *Malbranchea circinata* Sigler & Carmichael produced peptides, glycosylated anthraquinones, and tetralones with inhibitory properties against AG and PTP-1B; the peptide malbrancheamide was also active during an oral sucrose tolerance test (OSTT) in mice.[7] Finally, *Malbranchea albolutea* Sigler & Carmichael biosynthesizes ardeemin derivatives with potent PTP-1B inhibitory effects.[8]

Malbranchea dendritica Sigler & Carmichael is a fungus isolated from soil worldwide.[9] From the chemical and pharmacological point of view, this species has not been investigated. However, other *Malbranchea* species, in addition to those indicated above, biosynthesize different types of

Received: July 13, 2021
Accepted: August 12, 2021
Published: August 25, 2021

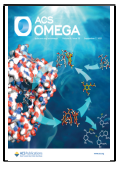

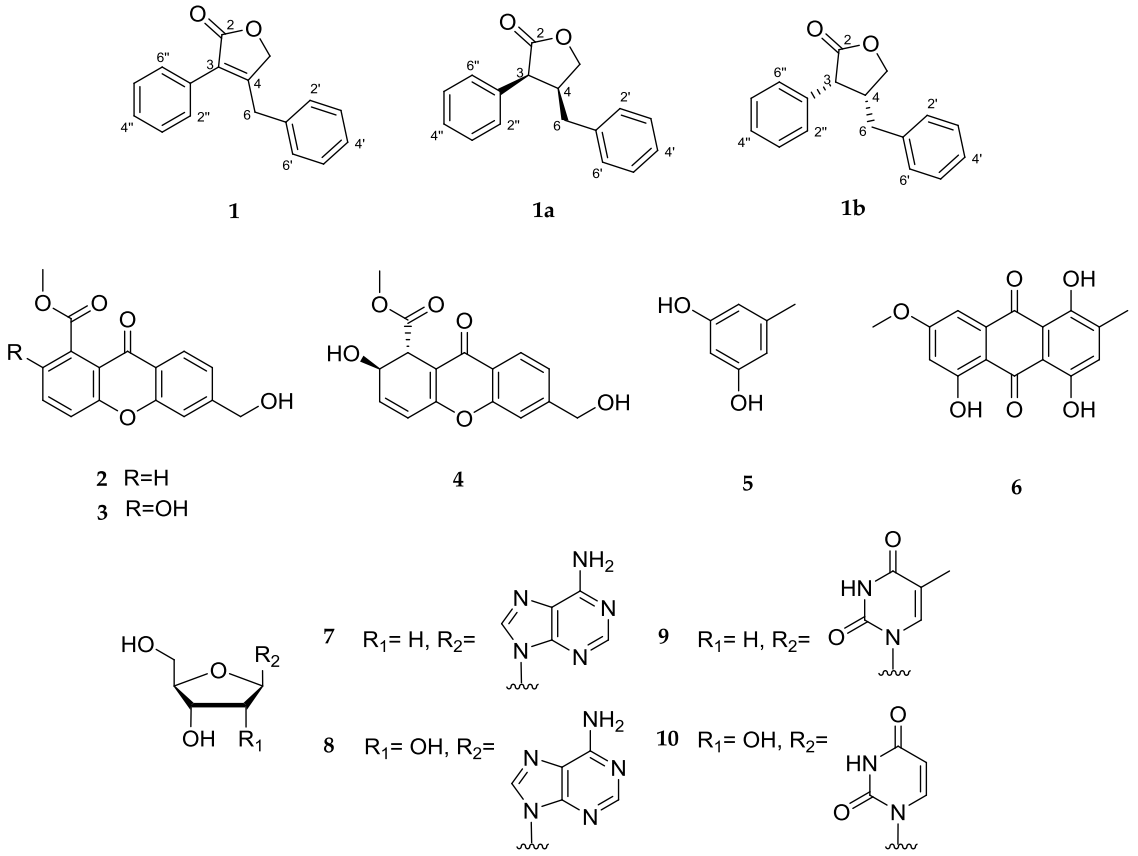

Figure 1. Chemical structures of compounds **1**−**10** isolated from the fungus *M. dendritica* and derivatives.

bioactive compounds, including peptides,[10−13] sesquiterpenoids,[14,15] polyketides,[5,6] benzoquinones and hydroquinones,[16,17] triterpenoids,[18] anthrasteroids,[19] aromatic compounds,[20,21] and pyrrole alkaloids.[22]

Herein, we report a few PTP-1B and AG inhibitors from *M. dendritica* obtained from the American Type Culture Collection (ATCC, strain 34527), including their activities, kinetic behavior, drug-likeness, and other *in silico* properties. The identity of the fungus was also confirmed using molecular sequencing.

RESULTS AND DISCUSSION

Fungal Strain and Identification. The identity of the type strain of *M. dendritica* ATCC 34527 (UAMH 2731, CBS2731, DPG141) was confirmed using molecular sequencing of the ITS rDNA (ITS1, 5.8S, and ITS2) using the primer combination of ITS1F and ITS4.[23,24] Results of the BLAST search and maximum likelihood analysis with IQ-Tree (Figure S1) confirm that strain ATCC 34527 is *M. dendritica* (Onygenales; Onygenaceae; Ascomycota).

Isolation of Compounds 1−10. A $CHCl_3$−MeOH extract from a potato dextrose broth (PDB) static culture of *M. dendritica* showed activity against yeast AG and PTP-1B, with an inhibition of 76 and 30% at 1000 ppm, respectively. Sephadex purification of the active extract led to two major fractions (F1 and F2). F1 yielded pure compound **1**, identified by nuclear magnetic resonance (NMR) and spectrometric analyses (Figures S2 and S3 and Table S1), as gymnoascolide A, a vasodilating γ-butenolide previously isolated from *Malbranchea filamentosa*[20,21] and *Gymnoascus reessii* Baran.[25] The second fraction (F2) was subjected to high-performance liquid chromatography (HPLC) analysis, which resulted in the isolation of the xanthones sydowinin A (**2**), sydowinin B (**3**),[26] AGI-B4 (**4**),[27] and the polyketide orcinol (**5**).[28] Compounds **2**−**4** have been isolated from *Aspergillus sydowii* (Bainier & Sartory) Thom and Church,[26,29] *Engyodontium album* (Limber) de Hoog,[30] *Neosartorya fischeri* (Wehmer) Malloch & Cain,[31] and *Arthrinium* sp.,[32] and compound **5** from *Trichoderma atroviride* Karsten sensu Bissett[33] and *Aspergillus sclerotiorum* G.A. Huber.[34] Their spectral properties agreed with those previously reported (Figures S4−S11 and Tables S2−S5).

From the inactive barley-based solid culture of *M. dendritica*, the natural pigment erythroglaucin (**6**)[20] and the nucleosides deoxyadenosine (**7**), adenosine (**8**), thymidine (**9**), and uridine (**10**) were isolated and identified by comparison of their NMR data (Figures S12−S19 and Tables S6−S9) with those in the literature;[31] in addition, thymidine (**9**) was identified by X-ray diffraction analysis (Figure S20). All isolated compounds are shown in Figure 1. This type of finding is common since the variation of the culture conditions led to the production of different metabolites.

Evaluation of Compounds 1−5 against Yeast AG. Compounds **1**−**5** were evaluated against yeast AG using a spectrophotocolorimetric assay,[6,7] but only **1** exhibited an important inhibitory activity (IC_{50} = 0.556 ± 0.009 mM) comparable to that achieved by acarbose (IC_{50} = 0.403 ± 0.010 mM). Kinetic experiments were performed to determine the type of inhibition of **1** against yeast AG. Thus, substrate saturation curves at different concentrations of **1** were performed to obtain a double reciprocal (Lineweaver−Burk) plot (Figure 2), as described in the Experimental Section. This

https://doi.org/10.1021/acsomega.1c03708
ACS Omega 2021, 6, 22969−22981

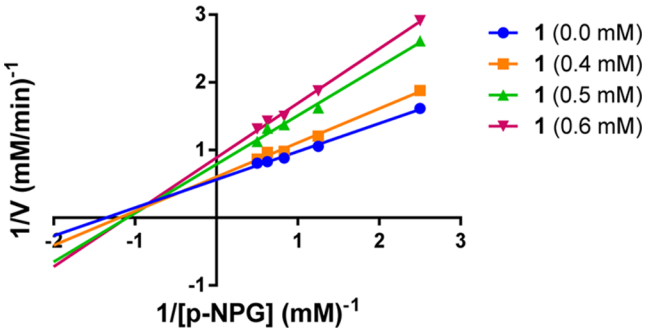

Figure 2. Lineweaver–Burk plot of yeast AG inhibition at different concentrations of gymnoascolide A (**1**).

plot showed a typical mixed-type inhibition, with the interception of the lines in the superior left quadrant; a difference in both the slope and *y*-intercept was observed, and when the inhibitor concentration increased, V_{max} decreased and K_m increased.[35] Calculated parameters V_{max}, K_m, and K_i were 1.720 mM/min, 0.6426 mM, and 0.7433 mM, respectively. The nonlinear regression (r^2 = 0.9546) for the Michaelis–Menten (Figure S21) reinforced the mixed type of inhibition.

***In Vivo* Evaluation of 1 during an Oral Sucrose Tolerance Test.** Compound **1** was also evaluated during an oral sucrose tolerance test (OSTT) in CD-1 normoglycemic mice (Figure 3), since yeast AG inhibition does not always correlate well with AG mammal inhibition. The OSTT monitors a reduction in glucose absorption associated with AG inhibition by measuring blood glucose after sucrose administration with and without the inhibitor.[36] During this experiment, compound **1** induced an important reduction of the postprandial peak at the doses of 5.16 and 10 mg/kg, and the antihyperglycemic effect lasted during the experiment. This effect was similar to that observed for acarbose (5 mg/kg), a well-known AG inhibitor used as a positive control.

Compound **1** was further analyzed for its antidiabetic potential during an oral glucose tolerance test (OGTT)[37] (3.16–10 mg/kg, p.o.) in normal mice, but only at the dose of 5.62 mg/kg, the postprandial peak decreased similarly to metformin (200 mg/kg). Thus, compound **1** might also improve insulin sensitivity (Figure S22).

Drug-Likeness, Pharmacokinetics, Medicinal Chemistry Friendliness, and Toxicity of Compounds 1, 1a, and 1b. Considering the good activity shown by compound **1** in the OSTT along with its antihypertensive potential,[20] the drug-likeness of this lactone was analyzed using SwissADME[38] and Osiris Property Explorer[39] free software.

The physicochemical properties of **1** were predicted, and the results are summarized in Figure S23 as a bioavailability radar plot. In the radar graphic, the pink area represents the optimal range for each property of a good drug, and the red line represents the values of the six calculated properties affecting its oral bioavailability. According to the results of Figure 4, compound **1** has good properties in terms of lipophilicity, size, polarity, insolubility, and flexibility but showed a large fraction of unsaturation.

The pharmacokinetic analysis predicted that compound **1** has a high chance of passively permeating the gastrointestinal (g.i.) and the blood–brain (BBB) barriers. In addition, compound **1** was not a substrate of the permeability glycoprotein (P-gp), a multidrug resistance protein that actively ejects xenobiotics out of cells. These results were graphically represented using the BOILED-Egg model (Figure S24). The predicted results also revealed that **1** has higher opportunities to be a CYP450 inhibitor of the isoforms CYP1A2, CYP2C19, and CYP2D6 (Figure S23), which might indicate adverse drug interactions with drugs that are substrates of this isoenzymes.

On the other hand, medicinal chemistry analysis, showed that compound **1** might be a good drug candidate because the results showed no pan-assay interference structural fragments (PAINS),[40] Brenk alerts,[41] or lead-likeness violations.[42] Furthermore, its synthetic accessibility is very good. Compound **1** also showed an orally bioavailable score of 0.55 and followed five drug-likeness rules, namely, Lipinski,[43] Egan,[44] Veber,[45] Muegge,[46] and Ghose.[47]

The toxicity risk assessment was estimated using the Osiris Property Explorer and the results anticipated no mutagenicity, tumorigenicity, or irritating or reproductive effects (Figure S25). Further, during the *in vivo* studies with compound **1**, no behavioral changes or irritating effects were observed in the mice.

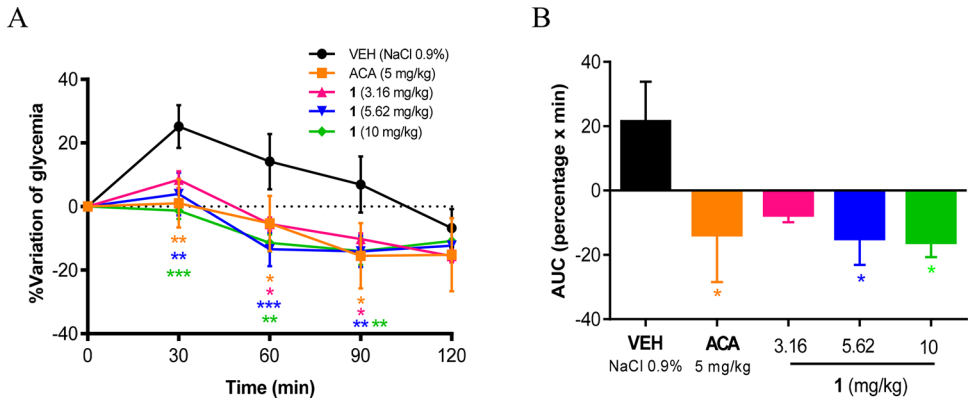

Figure 3. (A) Effect of compound **1** (3.16–10 mg/kg, p.o.) on blood glucose levels in normoglycemic mice during an OSTT. (B) Area under the curve (AUC) obtained from temporal curves. VEH: vehicle and ACA: acarbose. Each point or bar represents the mean ± SEM for six mice in each group. *p < 0.05, **p < 0.01, and ***p < 0.001 represent significantly different two-way ANOVA followed by Dunnett's test for comparison with respect to the vehicle control at the same time (panel A) or ANOVA followed by Dunnett's test for comparison with respect to the vehicle control (panel B).

https://doi.org/10.1021/acsomega.1c03708
ACS Omega 2021, 6, 22969–22981

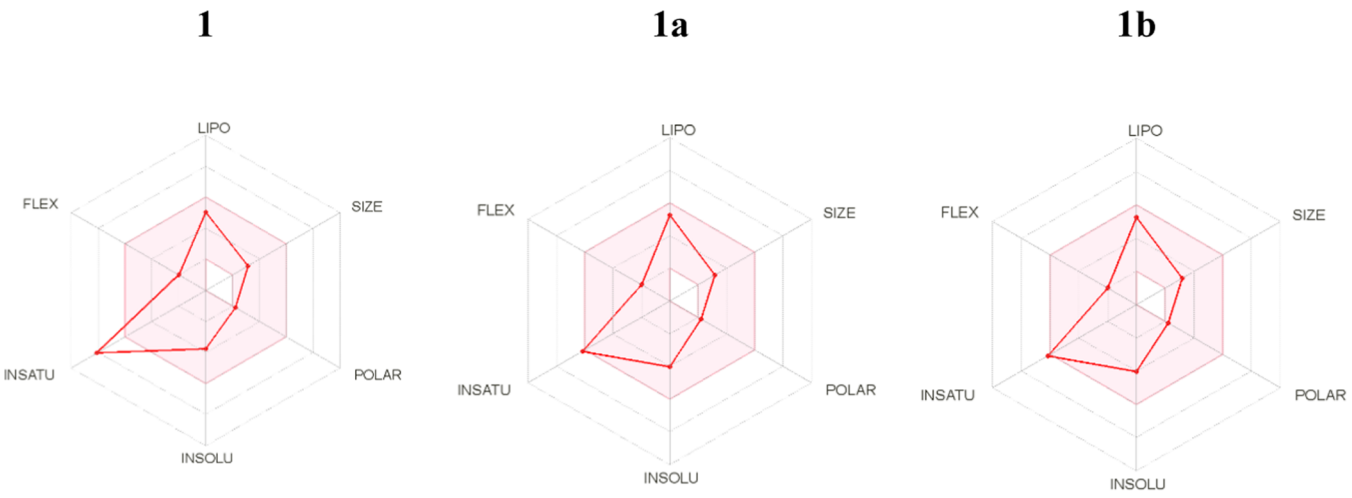

Figure 4. Bioavailability radar plot of compounds **1**, **1a**, and **1b** using the free web tool SwissADME.

To improve the medicinal chemistry properties of **1**, we decided to eliminate one unsaturation from its α,β-unsaturated lactone. Experimentally it can be achieved by catalytic hydrogenation using Pd/C. With the syn addition of hydrogen during this reaction, which takes place on the catalyst's surface, only two products, namely, **1a** and **1b**, might be obtained. Thus, **1a** and **1b** were subjected to the same theoretic analyses as **1**, and the results are summarized in the Supporting Information (Figures S26 and S27).

In general, **1a** and **1b** showed excellent pharmacokinetic and drug-likeness profiles. The bioavailability radar plots of both compounds showed no outliers (Figure 4), projecting better bioavailability than the parent compound **1**. Regarding the medicinal chemistry properties, a slight variation of XLOGP3 was foreseen, but the consensus log *P* remained less than 3.5. The Osiris Property Explorer also predicted no mutagenicity, tumorigenicity, or irritating or reproductive effects for compounds **1a** and **1b** (Figure S28).

Semisynthesis of Compounds 1a and 1b. To obtain a derivative less unsaturated, compound **1** was catalytically (Pd/C) reduced according to the procedure summarized in the Experimental Section. The reaction was monitored by GC–MS analysis (Figure S29), which revealed that the reaction yielded an enantiomeric mixture (8:2) of **1a** and **1b**, consistent with the syn addition of hydrogen to the double bond. The small value of the optical rotation $[\alpha]_D^{20} = -4$ (c = 1, MeOH) shows an enantiomeric excess of one of the two possible enantiomers. The enantiomeric mixture showed an exact mass of 253.12207 $[M + H]^+$ consistent with a molecular formula of $C_{17}H_{17}O_2$ and was clearly identified by NMR analysis (Table 1 and Figures S30 and S31). The main differences with the NMR of gymnoascolide A (**1**) were the absence of the signals for the double bond δ_C 159.8 (C-4) and 127.6 (C-3); instead, signals for two methines at C-3 and C-4 in δ_H/δ_C 4.06/50.3 and 3.08/34.7, respectively, were observed (Table 1), and the carbonyl carbon (δ_C 177.2) chemical shift was paramagnetically shifted due to the elimination of the double bond.

To determine which of the two enantiomers predominated in the mixture, the ECD of the 3*S*,4*S* (**1a**) and the 3*R*,4*R* (**1b**) enantiomers were calculated using a DFT B3LYP level of theory and compared with the experimental spectrum. Figure 5 depicts the comparison of three spectra; the sign and shape of the Cotton effects of the experimental spectrum is consistent with a predominancy of the 3*R*,4*R* (**1b**) enantiomer in the mixture.

Table 1. ^{1}H (400 MHz) and ^{13}C (100 MHz) NMR Data of Compound 1a/1b in $CDCl_3$

position	δ_C	δ_H[a] (J in Hz)
2	177.2	
3	50.3	4.06 d (8.2)
4	34.7	3.08 m
5	70.3	4.14 d (5.3, 9.3)
		4.26 d (6.4, 9.3)
6	42.7	2.45 dd (4.8, 14.1)
		2.20 dd (11.4, 14.1)
1′	138.6	
2′, 6′	129.0	7.02 br d (7.1)
3′, 5′	128.8	7.26 m
4′	126.8	7.20 m
1″	133.5	
3″, 5″	128.8	7.26 m
4″	128.0	7.34 m
2″, 6″	129.4	7.39 m

[a]Assigned with HSQC. Most aromatic protons are in the range of δ_H 7.2–7.39.

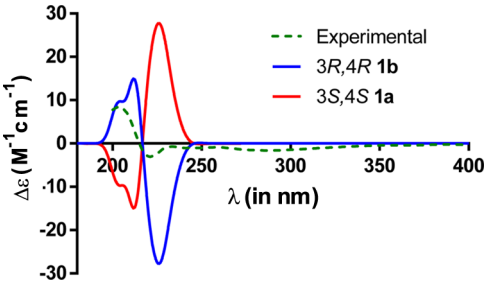

Figure 5. Comparison of the experimental ECD spectrum of the mixture **1a**/**1b** (green dotted line) with calculated spectra for the enantiomers 3*S*,4*S* (red) and 3*R*,4*R* (blue).

Evaluation of Compound 1a/1b against the Activity of Yeast AG. The unsaturated enantiomeric mixture **1a**/**1b** was evaluated against yeast AG, and the IC_{50} obtained was 0.396 ± 0.003 mM. This result shows a slight improvement in bioactivity compared to the parent compound. Kinetic experiments were also performed and compound **1a**/**1b**

https://doi.org/10.1021/acsomega.1c03708
ACS Omega 2021, 6, 22969−22981

retained the mixed-type inhibition as **1** (Figure 6). Calculated parameters V_{max}, K_m, and K_i were 1.447 mM/min, 0.5361 mM, and 0.6984 mM, respectively. The Michaelis–Menten graph (nonlinear regression for the mixed-type inhibition r^2= 0.9397) is shown in Figure S32.

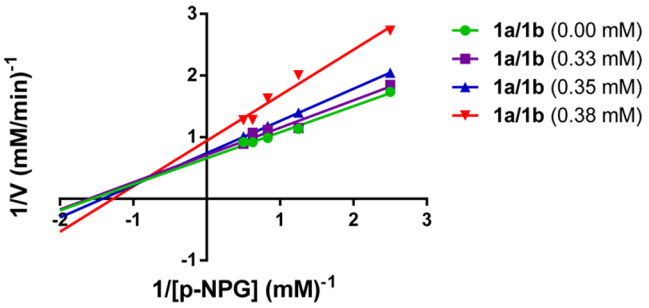

Figure 6. Lineweaver–Burk plot of yeast AG inhibition at different concentrations of compound **1a**/**1b**.

Docking Studies of 1, 1a, and 1b. Docking analysis of compound **1** and its analogs **1a** and **1b** was performed using two different enzymes: yeast isomaltase (pdb: 3A4A) considering that kinetic analyses were performed with this enzyme, and the C-terminal subunit of human maltase-glucoamylase (pdb: 3TOP) bearing in mind the *in vivo* results. The results are shown in Figures 7 and 8 and Tables 2 and 3, which include the type of interactions, binding amino acids, binding energies, and calculated inhibition constants. In all cases, the compounds bind to the noncatalytic site of the enzymes.

For yeast AG, the three compounds **1**, **1a**, and **1b** bind to an allosteric site[48] with almost identical binding energies (Table 2), and this information supports the kinetics experiments carried out with this enzyme *in vitro*. In the case of the C-terminal subunit of human maltase-glucoamylase, compound **1** attached to a different site from that of its derivatives **1a** and **1b**; in each case the binding site was different to the catalytic region, and the binding energies were slightly better than that of acarbose used as the positive control (Table 3).

The type of interactions **1**, **1a**, and **1b** displayed with all enzymes were predominantly hydrophobic. However, in the case of the maltase-glucoamylase enzyme, π stacking and salt bridge interactions were also observed (Figures 7 and 8 and Tables 2 and 3). The interactions of acarbose are shown in Figures S33 and S34.

PTP-1B Inhibitory Activity. Compounds **1**–**5** were evaluated against PTP-1B, but only compound **3** moderately inhibited the enzyme with an IC_{50} of 0.081 ± 0.004 mM; ursolic acid (UA) was used as the positive control (IC_{50} = 0.006 ± 0.0002 mM). Kinetic analysis revealed that xanthone **3** inhibited PTP-1B in a noncompetitive fashion (the interception of the lines was observed at the *x*-axis); the estimated K_i was 0.02745 mM (Figure 9). Accordingly, a decrease in V_{max} (1.308 mM/min) but no change in the K_m parameter (1.360 mM) was observed. Furthermore, the r^2 value (0.9978) estimated in the nonlinear regression analysis of the Michaelis–Menten graph (Figure S35) endorsed a noncompetitive type of inhibition.

Docking and Molecular Dynamics Studies of Compound 3. Docking analysis of compound **3** was performed with a human recombinant PTP-1B (pdb: 1T49). As shown in Figure 10, **3** might bind in a well-known allosteric site[49,50] and could display hydrophobic, H bonds and π-stacking interactions with the amino acids in the site (Table 4). The positive control, ursolic acid also binds to the allosteric site, and interactions of this compound are shown in Figure S36.

The molecular dynamics (MD) results are also summarized in Table 4 and Figure 11. The complex of compound **3**-enzyme resulted in a negative ΔG value. The calculated RMSD for the complex of **3**, UA, and PTP-1B (Figure 12) indicated that they remain stable throughout the simulation time.

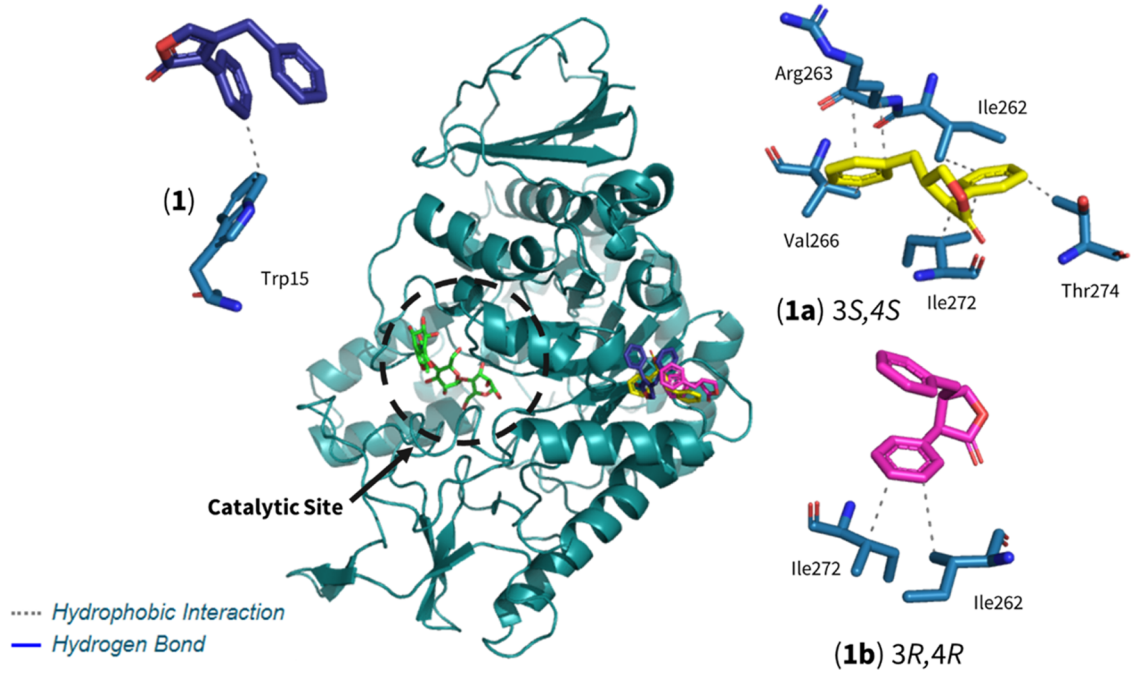

Figure 7. Structural models of the binding sites of the yeast AG-ligand complexes (pdb: 3A4A). In the center, the protein α-glucosidase is shown in light blue cartoon, and compounds are shown in blue sticks (**1**), yellow sticks (**1a**, 3S,4S), magenta sticks (**1b**, 3R,4R), and green sticks (acarbose).

https://doi.org/10.1021/acsomega.1c03708
ACS Omega 2021, 6, 22969–22981

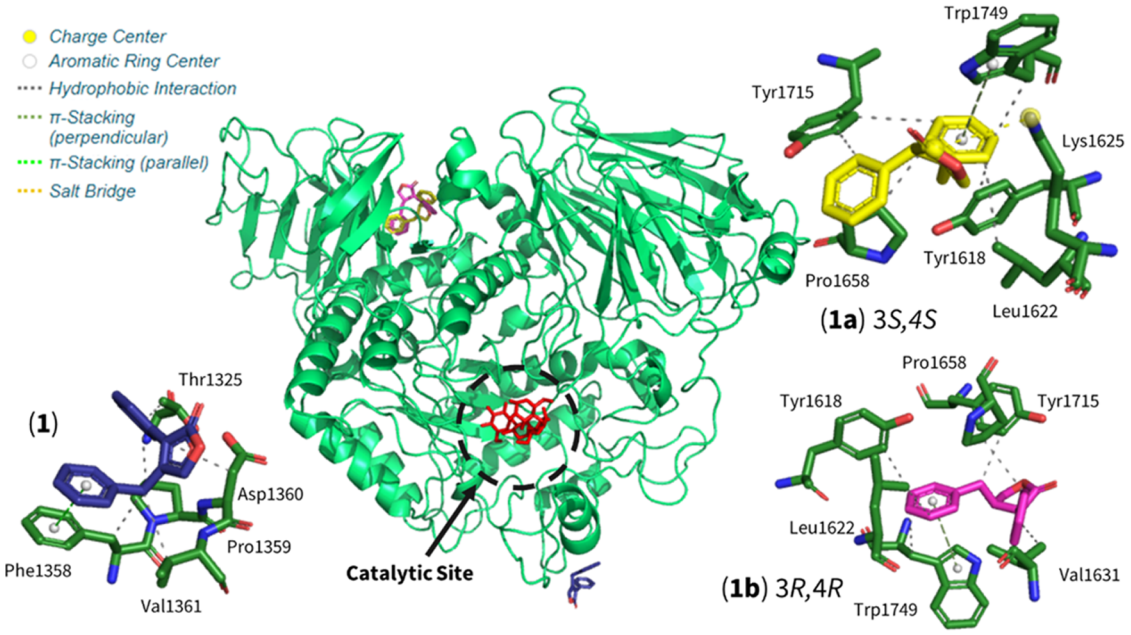

Figure 8. Structural models of the binding sites of the C-terminal subunit of human maltase-glucoamylase (pdb: 3TOP). In the center, the protein α-glucosidase is shown in green cartoon and compounds are shown in blue sticks (**1**), yellow sticks (**1a**, 3S,4S), magenta sticks (**1b**, 3R,4R), and red sticks (acarbose).

Table 2. Docking Analysis Results from Compounds 1, 1a, 1b, and Acarbose in Yeast AG (pdb: 3A4A)

compound	K_i (μM)	EB (kcal/mol)	interacting residues
1	32.53	−6.1	Trp15[a]
1b (3R,4R)	38.54	−6.0	Ile262[a], Ile272[a]
1a (3S,4S)	9.94	−6.8	Ile262[a], Arg263[a], Val266[a], Ile272[a], Thr274[a]
acarbose	0.78	−8.3	Tyr155[c], Glu274[c], Gln276[c], His277[c], Asp304[c], Thr307[c], Arg312[c], Arg439[b]

[a]Hydrophobic interaction. [b]Hydrogen bond. [c]Salt bridge.

Table 3. Docking Analysis Results from Compounds 1, 1a, 1b, and Acarbose in the C-Terminal Subunit of Human Maltase-Glucoamylase (pdb: 3TOP)

compound	K_i (mM)	EB (kcal/mol)	interacting residues
1	54.08	−5.8	Thr1325[a], Phe1358[a,b], Pro1359[a], Asp1360[a], Val1361[a]
1b (3R,4R)	16.52	−6.5	Tyr1618[a], Leu1622[a], Val1631[a], Pro1658[a], Tyr1715[a], Trp1749[a,b]
1a (3S,4S)	5.98	−7.1	Tyr1618[a], Leu1622[a], Lys1625[c], Pro1658[a], Tyr1715[a,b]Trp1749[a,b]
acarbose	23.18	−6.3	Trp1355[a], Phe1559[a], Asp1157[d], Lys1460[d], Arg1510[d], Asp1526[d], His1584[d], Thr1528[d]

[a]Hydrophobic interaction. [b]π-Stacking. [c]Salt bridge. [d]Hydrogen bond.

These findings are consistent with the *in vitro* assays. Thus, compound **3** binds to the allosteric site of the enzyme in a noncompetitive fashion. Therefore, the formation of the complex and the formation of the complex between **3** and PTP-1B could result in the inhibition of the enzyme.

Drug-Likeness, Pharmacokinetics, Medicinal Chemistry Friendliness, and Toxicity of Compounds 1−10.

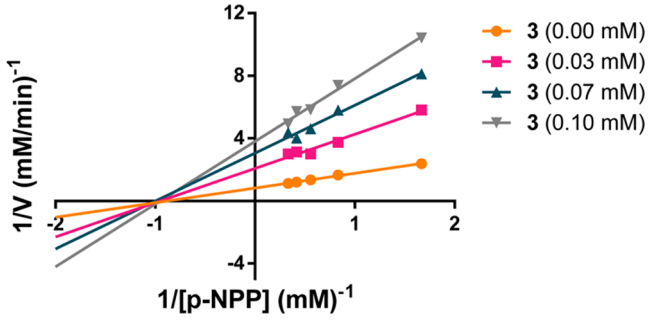

Figure 9. Lineweaver−Burk plot of PTP-1B inhibition at different concentrations of the substrate of sydowinin B (**3**).

Compound **3** was also subjected to bioinformatic analyses with SwissADME[38] and Osiris Property Explorer[39] free software.

The predicted physicochemical properties depicted in the bioavailability radar plot (Figure S37) showed an outlier at the unsaturation parameter. The pharmacokinetic calculations projected were favorable since **3** was not a substrate of P-gp and could not pass through the BBB but it was permeable to g.i. membranes (Figure S38). In addition, this compound would not inhibit any CYP450 isoforms. Xanthone **3** followed the five drug-likeness rules and showed no PAINS or lead-likeness violations; however, a Brenk alert was found because of its polycyclic backbone.

Finally, the Osiris Property Explorer was used to evaluate the toxicity risk for compound **3** and the results showed no mutagenicity or tumorigenicity effects, but a slight alert for irritating and reproductive effects (Figure S36) were foreseen.

CONCLUSIONS

In summary, gymonascolide A (**1**) demonstrated *in vivo*, *in vitro*, and *in silico* α-glucosidase inhibitory activity; its reduced derivatives **1a** and **1b** showed comparable *in vitro* activity as AG inhibitors, and according to their predicted drug-likeness

https://doi.org/10.1021/acsomega.1c03708
ACS Omega 2021, 6, 22969−22981

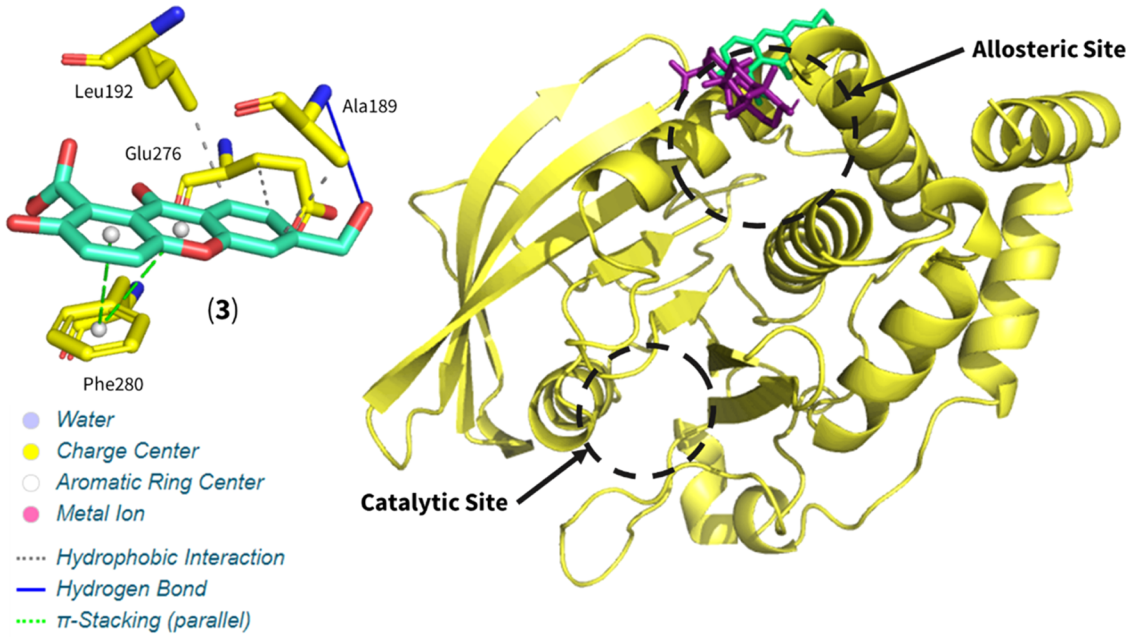

Figure 10. Structural models of the binding sites of PTP-1B-ligand complexes (pdb: 1T49). The protein is shown in yellow cartoon, compound **3** in blue sticks, and positive control (UA) in purple sticks.

Table 4. Docking and Molecular Dynamics Analysis Results from Compound 3 and UA in PTP-1B (pdb: 1T49)

compound	K_i (μM)	EB (kcal/mol)	ΔG (kcal/mol)	interacting residues
3	4.26	−7.3	−29.58 ± 3.71	Ala189[a,b], Leu192[a], Phe280[c], Glu276[a]
UA	27.47	−6.2	−24.99 ± 2.61	Phe196[a], Phe280[a], Ile281[a]

[a]Hydrophobic interaction. [b]Hydrogen bond. [c]π-Stacking.

and medicinal chemistry properties, they could be better lead compounds for the development of new drugs. Compound **1** might also favor insulin sensitivity of resistance according to an OGTT in mice. However, further investigation *in vivo* is required to demonstrate these hypotheses. Its vasodilating effect demonstrated by other authors might be useful in diabetic patients with cardiovascular complications. The xanthone sydowinin B (**3**) showed significant inhibitory activity against the enzyme PTP-1B; nevertheless, its predicted toxicological properties ruled out a further detailed investigation on this compound. As other *Malbranchea* species, *M.*

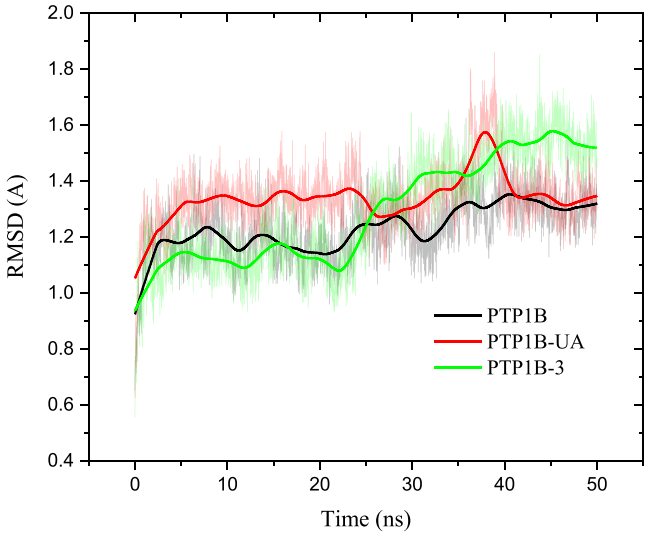

Figure 12. RMSD as a function of time of the PTP-1B-**3** and PTP-1B-UA complexes.

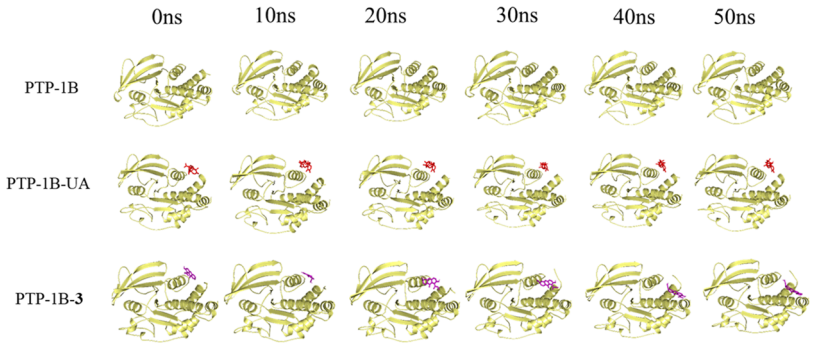

Figure 11. Structural models for molecular dynamics at the allosteric site of PTP-1B for compound **3** and UA.

https://doi.org/10.1021/acsomega.1c03708
ACS Omega 2021, 6, 22969−22981

dendritica demonstrated to be a good source of potential antidiabetic drugs.

EXPERIMENTAL SECTION

General Experimental Procedures. NMR spectra, including bidimensional, were recorded in CD_3OD, $CDCl_3$, or DMSO-δ_6 solution on a Bruker Avance III HD or Bruker BioSpin (Billerica, MA) spectrometer at either 700 or 400 MHz (^{1}H) and 175 or 100 MHz (^{13}C), using TMS as an internal standard. High-resolution mass spectra, HRMS (ESI-TOF$^+$), were acquired with a JEOL AccuTOF JMS-T100LC (Peabody, MA) spectrometer. Optical rotation was obtained with an Anton Paar MCP 150 polarimeter. Gas chromatography−mass spectrometry (GC−MS) determinations were made using an Agilent 5975C system equipped with a 30 m DB-5MS capillary column (0.25 mm i.d.; 0.25 mm). Preparative HPLC was carried out with a Waters instrument (Milford, MA) equipped with a 2535 pump and a 2998 photodiode array detector, using an XBridge Prep Shield RP-C18 (19.0 × 250 mm^2, 5 mm particle size) packed column, and different gradient systems of MeCN and 0.1% aqueous formic acid, at a flow rate of 17.06 mL/min. Control of equipment, data acquisition and processing, and management of chromatographic information were performed using the Empower 3 software package. Column chromatography (CC) was carried out on silica gel 60 (Merck, Darmstadt, Germany) or Sephadex LH-20 (GE Healthcare, Little Chalfont, Buckinghamshire, U.K.). Thin-layer chromatographic (TLC) analyses were performed on silica gel 60 F254 plates (Merck) and visualized using a $Ce_2(SO_4)_3$ (10%) solution in H_2SO_4.

Fungal Strain and Identification. *M. dendritica* (strain no. 34527) was obtained from ATCC (Manassas, VA). The lyophilized fungus was resuspended with sterile water and left overnight. Next, Potato Dextrose Agar (PDA) plates were inoculated with the suspended fungi and were continuously subcultured for preservation. The identity of the fungus was confirmed using molecular sequencing. Detailed methods for PCR amplification and sequencing were outlined previously.[51] A BLAST search with the fungi type and reference material database in NCBI GenBank using the ITS region suggested that ATCC 34527 displayed ≥99% sequence similarity with *M. dendritica* UAMH 2731 REFSEQ, NR_111141 (AY177310).[52] To place the strain ATCC 34527 in a phylogenetic framework, we downloaded all types and other sequences from various closely related *Malbranchea* and *Auxarthron* spp[53−55] and performed a Maximum Likelihood analysis using methods detailed recently.[8] ModelFinder[56] predicted TIM3e+I+G4 as the best fitting substitution model according to the Akaike Information Criterion.[57] The trimmed nucleotide alignment after removing ambiguous nucleotide positions with GBlocks[58,59] was then used to run the Maximum Likelihood analysis using IQ-Tree implemented using the program PhyloSuite with 5000 Ultrafast bootstrapping.[60−62] Only Ultrafast bootstrap values ≥95% for the clades were considered strongly supported. The BLAST search and Maximum Likelihood analysis with IQ-Tree (Figure S1) confirm that strain ATCC 34527 is *M. dendritica*. A new sequence data information was added to NCBI GenBank for the type strain with the accession number MZ486089.

Fermentation, Extraction, and Isolation of Compounds. *M. dendritica* was cultured in two different media, potato dextrose broth (PDB) and semisolid barley medium. First, the microorganism was cultured for 2 weeks in PDA plates; next, small cubes of solid agar were used as the seed for PDB media cultures (100 mL). These preinocula were cultured for 1 week and served as the seed for the medium-scale culture. In the first case, 6 L of PDB were inoculated and cultured in static conditions. On the other hand, the solid culture was carried out in Fernbach flasks containing barley media (100 g/200 mL of water).

For the liquid medium, the fungus was grown for 28 days and then it was exhaustively extracted with $CHCl_3$−MeOH (8:2); the resulting extract was evaporated *in vacuo*. The extract was resuspended in MeOH−MeCN (1:1) and partitioned with *n*-hexane (6 × 200 mL).

Defatted liquid medium extract (200 mg) was then fractionated with Sephadex CC using a mobile phase of CH_2Cl_2−MeOH (2:8); this resulted in two major fractions, F1 which resulted in pure compound **1** (60 mg) and the rest of the fractions were gathered in F2. F2 was then fractionated with preparative RP-HPLC using a gradient of MeCN-0.1% aqueous formic acid (30:70 to 85:15 in 20 min) to yield **2** (1 mg, t_R 11.0 min), **3** (4 mg, t_R 8.5 min), **4** (2 mg, t_R 5.5 min), and **5** (2 mg, t_R 13.5 min).

The solid medium culture was grown for 28 days and then it was macerated for 12 h with EtOAc, and at the end of that time, the solvent was evaporated to give the resulting extract. The total solid medium extract was then resuspended with MeCN−MeOH (1:1) and partitioned with *n*-hexane, and at this stage, compound **6** (5 mg) precipitated spontaneously. The defatted solid medium extract (900 mg) was then fractionated in silica gel CC using a gradient of *n*-hexane−$CHCl_3$−acetone, to yield 11 primary fractions. Fraction 8 (30 mg) was then eluted in a preparative TLC, with a mobile phase of EtOAc−MeOH (85:15) to yield compounds **7** (2 mg), **8** (1.5 mg), **9** (3 mg), and **10** (1.5 mg).

Synthesis of Compound 1a/1b. A mixture of compound **1** (0.17 mmol) in EtOAc (1 mL) and Pd/C (10 mol %) was stirred under an atmospheric pressure of hydrogen for 20 h. The solution was then filtered and washed exhaustively with EtOAc, resulting in 34 mg of the crude reaction product.[63] The crude product was then purified by silica gel chromatography CH_2Cl_2-Hex (9:1), to yield 30 mg of compound **1a/1b** (82% yield) (Scheme 1).

Scheme 1. Reduction of Compound 1

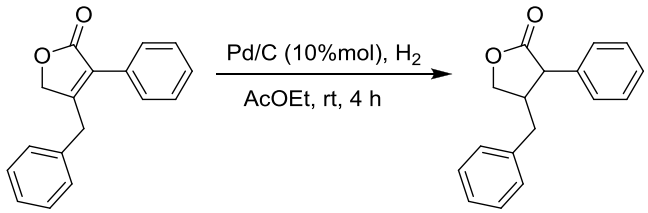

Dihydrogymnoascolide A (**1a/1b**): a colorless glassy solid; $[\alpha]_D^{20}$ = −4 (*c* = 1, MeOH); UV λ_{max} (log ε) 206.9 (4.85) nm; IR (FTIR) ν_{max}: 3356, 1766, 1450, 1170, 697 cm^{-1}; ^{1}H NMR (400 MHz, $CDCl_3$), ^{13}C NMR (100 MHz, $CDCl_3$), see Table 1. HRESIMS *m*/*z* 253.12207 [M + H]$^+$, calcd. for $C_{17}H_{17}O_2$ 253.12285 Δppm = 3.1.

***α*-Glucosidase Activity Assay.** The enzymatic assay was carried out using our previously reported method.[6,7] Briefly, the fungal extract, compounds **1** and **1a/1b**, and the positive

https://doi.org/10.1021/acsomega.1c03708
ACS Omega 2021, 6, 22969−22981

control (acarbose) were dissolved in MeOH or phosphate buffer solution (100 mM, pH = 7.0). Aliquots of 0−10 μL of testing materials (triplicated) were incubated for 10 min with 20 μL of 1 U/mL α-glucosidase from yeast AG enzyme solution. After incubation, 10 μL of *p*-nitrophenyl-α-D-glucopyranoside (*p*-NPG 5 mM) was added and further incubated for 20 min at 37 °C, and at the end of this time the absorbance was measured at 415 nm. The inhibitory activity was determined as a percentage compared to the blank according to the following equation

$$\%\alpha - \text{GHY} = \left(1 - \frac{A_{415b}}{A_{415c}}\right) \times 100\%$$

where %α-GHY is the percentage of inhibition, A_{415c} is the corrected absorbance of the samples under testing ($A_{415end} - A_{415initial}$), and A_{415b} is the absorbance of the blank ($A_{415endblank} - A_{415initialblank}$). All assays were performed in triplicate. The IC_{50} was calculated by regression analysis, using the following equation

$$\%\ \text{inhibition} = \frac{A_{100}}{1 + \left(\frac{I}{IC_{50}}\right)^s}$$

where A_{100} is the maximum inhibition, I is the inhibitor concentration, IC_{50} is the concentration required to inhibit the activity of the enzyme by 50% ± SD, and s is the cooperative degree.[64]

α-Glucosidase Kinetic Studies. Kinetic analyses were performed for compounds **1** and **1a**/**1b**. The assay was carried out using different concentrations of yeast AG inhibitors (0.4, 0.5, and 0.6 mM for compound **1** and 0.33, 0.35, and 0.38 mM for **1a**/**1b**) with different concentrations of the substrate (0.4−2 mM *p*-NPG). The results of these substrate saturation curves can be transformed into a double reciprocal (Lineweaver−Burk) plot. The equation for this plot is the following

$$\frac{1}{V} = \left(\frac{K_m}{V_{max}}\right)\left(\frac{1}{[S]}\right) + \frac{1}{V_{max}}$$

The slope for this equation is K_m/V_{max}, the point at which the linear regression line intersects the y-axis is numerically equivalent to $1/V_{max}$, and the point at which it intersects the x-axis is $-1/K_m$. Thus, a Lineweaver−Burk plot provides identifiable x- and y-intercepts where the kinetic parameters V_{max} and K_m can be obtained.[35] The changes in slope and axis intercepts are characteristic for each type of inhibitor. Kinetic parameters (V_{max}, K_m, K_i) were obtained by the nonlinear regression fit analysis using GraphPad Prism version 6 for Windows (GraphPad Software, San Diego, CA, www.graphpad.com).

***In Vivo* Oral Sucrose and Glucose Tolerance Tests.** CD-1 male mice, aged 4 weeks, were obtained from Universidad Autónoma Metropolitana Unidad Xochimilco (approved protocol 182). Animals were kept under controlled temperature (25 °C), and a 12 h light/dark cycle, and water and food pellets (Lab Diet 5001 Rodent diet) were provided ad libitum. The experimental animal protocol followed the recommendations of the Mexican Official Norm for Animal Care and Handling (NOM-062-ZOO-1999) and was in conformity with the International Ethical Guidelines for the Care and Use of Laboratory Animals. The Ethical Committee for the Use of Animals in Pharmacological and Toxicological Testing, Facultad de Química, UNAM (FQ/CICUAL/403/20), approved the protocol on February 5, 2020.

Mice were fasted 4 h before experimental handling, and they were separated into 5 groups (I−V) of 8 animals each. All groups were administered p.o.; the treatments were given as follows, group I, the vehicle solution (VEH, saline solution with 1% tween 80); group II, the positive control (acarbose, ACA, 5 mg/kg in the case of OSTT or metformin, MET, 200 mg/kg in the case of OGTT), and groups III−V, compound **1** at three different doses: 3.16, 5.62, and 10 mg/kg. Thirty minutes after the administration of the treatment, an oral sucrose (1.5 g/kg) or glucose (1 g/kg) load was given to all groups. Blood glucose levels were determined at 30, 60, 90, and 120 min after the administration of the carbohydrate. The percentage of glycemic variation (%) was determined with respect to the basal level as follows

$$\%\ \text{variation of glycemia} = \frac{G_t - G_i}{G_i} \times 100\%$$

where G_i is the basal glycemia and G_t is the different glycemia values after treatment administration.

Statistical Analysis. Data are expressed as the mean ± standard error of the mean. Statistical significance differences were ascertained by means of one or two-way ANOVA followed by Dunnett's test for comparison with respect to the vehicle control. GraphPad Prism software (version 6) was used for statistical analysis.

Protein Tyrosine Phosphatase 1B (PTP-1B) Activity Assay. A recombinant human protein tyrosine phosphatase 1B (PTP-1B) was used.[8] The fungal extract, isolated compounds, and positive control (ursolic acid) were dissolved in DMSO or tris buffer solution (100 mM pH = 6.8). Aliquots of 0−10 μL of testing materials (triplicated) were incubated for 5 min with 20 μL of 1.56 mg/mL PTP-1B enzyme solution. After incubation, 10 μL of *p*-nitrophenyl phosphate (*p*-NPP, 3 mM) was added and further incubated for 20 min at room temperature; the absorbance was measured at 415 nm. The inhibitory activity was determined as follows

$$\%\text{PTP} - 1\text{B} = \left(1 - \frac{A_{415b}}{A_{415c}}\right) \times 100\%$$

where %PTP-1B is the percentage of inhibition, A_{415c} is the corrected absorbance of the samples under testing ($A_{415end} - A_{415initial}$), and A_{415b} is the absorbance of the blank ($A_{415endblank} - A_{415initialblank}$). All assays were performed in triplicate. The IC_{50} was calculated by regression analysis, using the following equation

$$\%\ \text{inhibition} = \frac{A_{100}}{1 + \left(\frac{I}{IC_{50}}\right)^s}$$

where A_{100} is the maximum inhibition, I is the inhibitor concentration, IC_{50} is the concentration required to inhibit the enzyme activity by 50% ± SD, and s is the cooperative degree.[64]

PTP-1B Kinetic Studies. Kinetic analysis was performed for compound **3**. The assay was carried out using different concentrations of the inhibitor (0.03, 0.07, and 0.1 mM) with varying concentrations of *p*-NPP (0.6−3 mM). Kinetic parameters (V_{max}, K_m, K_i) were obtained by the nonlinear regression fit analysis using GraphPad Prism version 6 for

https://doi.org/10.1021/acsomega.1c03708
ACS Omega 2021, 6, 22969−22981

Windows (GraphPad Software, San Diego, CA, www.graphpad.com).

ECD Calculations. Minimum energy structures from the two compounds **1a** and **1b** were built using Spartan' 08 software (Wavefunction Inc., Irvine, CA). Conformational analysis was carried out with the Monte Carlo search protocol under MMFF molecular mechanics approximation. Conformers with relative energy under 5 kcal/mol were submitted to Gaussian 09 program (Gaussian Inc., Wallingford, CT) calculation for geometry optimization using the DFT B3LYP/DGTZVP level of theory and default model for MeOH as the solvent. The same DFT method in MeOH was employed for ECD calculations using the DFT-minimized conformers. The calculated excitation energy (nm) and rotatory strength (R) in dipole velocity (R_{vel}) and dipole length (R_{len}) forms were simulated into an ECD curve. The calculated and weighted ECD curves were all generated using SpecDis 1.71.[65]

Docking Protocol. Docking analysis was done using α-glucosidase yeast AG (pdb: 3A4A), the C-terminal subunit of human maltase-glucoamylase (pdb: 3TOP), and PTP-1B from *Homo sapiens* (pdb: IT49). Structures **1**, **1a**, **1b**, and **3** were constructed and minimized using Spartan software. AutoDockTools 1.5.4 (http://mgltools.scripps.edu/) was used to prepare the pdb files of both enzymes and compounds. Polar hydrogen atoms and the Kollman united-atom partial charges were added to the protein structures, while Gasteiger−Marsili charges and rotatable groups were automatically assigned to the structures of the ligands. First, a blind docking was carried out with AutoDock4 version 4.2 (http://autodock.scripps.edu/), and the grid box was set at 126 Å × 126 Å × 126 Å in the x, y, and z dimensions with a spacing of 0.5 Å; default parameters for the Lamarckian genetic algorithm were also used. For the docking refinement, a smaller grid was utilized with dimensions of 60 Å × 60 Å × 60 Å with a spacing of 0.375 Å, centered at the previously identified ligands' binding site. Conformational states were evaluated with AutoDockTools using cluster analysis. The visualization of the best conformational states was achieved using PyMOL (The PyMOL Molecular Graphics System, Version 2.0 Schrödinger, LLC) and Protein−Ligand Interaction Profiler (PLIP) software.[66]

Molecular Dynamics Simulation. All of the structural complexes were validated with the pdb4amber script previously starting the preparation to generate suitable topologies from the LEaP module of AMBER 19.[67,68] In each case, the structure and complex were subjected to the following procedure: hydrogens and other absent atoms were added using the LEaP module with the leaprc.protein.ff19SB parameter set; K^+ counter ions were also included to neutralize the system. The complexes were solvated in an octahedral box of explicit TIP3P model water molecules localizing the box limits at 12 Å from the protein surface. Molecular dynamics (MD) simulations were performed at 1 atm and 315 K, maintained with the Berendsen barostat and thermostat, using periodic boundary conditions and particle mesh Ewald sums (grid spacing of 1 Å) for treating long-range electrostatic interactions with a 10 Å cutoff for computing direct interactions. The SHAKE algorithm was used to satisfy bond constraints, allowing the employment of a 2 fs time step for the integration of Newton's equations as recommended in the Amber package.[68,69] Amber leaprc.protein.ff19SB force field[70] parameters were used for all residues. All calculations were made using a graphic processing unit (GPU)-accelerated MD engine in AMBER (pmemd.cuda), a program package that runs entirely on CUDA-enabled GPUs.[71] The protocol consisted of performing a minimization of the initial structure, followed by 50 ps heating and pressure equilibration at 315 K and 1.0 atm pressure, respectively. Finally, the system is equilibrated with 500 ps before starting the production of MD. The production of the MD consisted of 50 ns for each complex. Frames were saved at 10 ps intervals for subsequent analysis. All analyses were done using the CPPTRAJ[72] part of AMBER 19 utilities and OriginPro 9.1. The calculations of RMSD were made considering the C, CA, and N. The charts were built with OriginPro 2018 SR1, and the trends were adjusted with the function processing smooth (method lowess span). VMD and PyMOL were used to visualize and create the images from the MD.

Bioinformatics Studies of Bioactive Compounds Using the SwissADME Tool and Osiris Property Explorer Software. Pharmacokinetic and drug-likeness properties of the active molecules were analyzed with the SwissADME online server (http://www.swissadme.ch/).[38] Physicochemical properties of compounds were collected and represented with the bioavailability radar, where the pink area embodies the optimal range of each property as plotted: lipophilicity (LIPO): −0.7 < XLOGP3 < +5.0; SIZE: 150 g/mol < MW < 500 g/mol; POLAR (polarity): 20 Å^2 < topological surface area (TPSA) < 130 Å^2; INSOLU (insolubility): 0 < log S (ESOL) < 6; INSATU (insaturation): 0.25 < fraction of Csp3 <1; and FLEX (flexibility): 0 < number of rotatable bonds < 9. Compounds with an optimal drug-likeness must have the red lines inside the pink area.

Passive human gastrointestinal absorption (g.i.), blood−brain barrier (BBB) permeation, susceptibility for permeability glycoprotein (P-gp) capacity, and interaction of molecules with five major isoforms of the human cytochromes P450 were predicted for bioactive compounds. Permeability information was summarized using the BOILED-Egg construction model, which was obtained via SwissADME software.

Medicinal chemistry properties such as pan-assay interference compounds (PAINS), Brenk alerts, lead likeness, and synthetic accessibility were also predicted using the software.

Osiris Property Explorer (http://www.organic-chemistry.org/prog/peo/) free software was used to predict mutagenicity, tumorigenicity, and irritative and reproductive effects of the bioactive compounds. The toxicity risk alerts obtained from the software must be taken into consideration because the absence of risk alerts does not mean a completely free of any toxic effect, but a risk alert also cannot be a fully reliable toxicity prediction.

■ ASSOCIATED CONTENT

Supporting Information

The Supporting Information is available free of charge at https://pubs.acs.org/doi/10.1021/acsomega.1c03708.

The phylogenetic tree for *M. dendritica*; NMR spectra of compounds **1**−**10** and **1a**/**1b**; ORTEP graph of compound **9**; Michaelis−Menten graphs for **1**, **1a**/**1b** and **3**; OGTT graph of compound **1**; physicochemical, pharmacokinetic, and toxicological predicted properties of compounds **1**, **1a**, **1b**, and **3**; GC−MS resulting chromatogram of the product of the catalytic reduction of compound **1**; and data concerning the docking analysis of acarbose and UA (PDF)

https://doi.org/10.1021/acsomega.1c03708
ACS Omega 2021, 6, 22969−22981

AUTHOR INFORMATION

Corresponding Author

Rachel Mata − *Facultad de Química, Universidad Nacional Autónoma de México, Ciudad de México 04510, Mexico;* orcid.org/0000-0002-2861-2768; Email: rachel@unam.mx

Authors

Daniela Rebollar-Ramos − *Facultad de Química, Universidad Nacional Autónoma de México, Ciudad de México 04510, Mexico*

Berenice Ovalle-Magallanes − *Facultad de Química, Universidad Nacional Autónoma de México, Ciudad de México 04510, Mexico*

Juan Francisco Palacios-Espinosa − *Departamento de Sistemas Biológicos, División de Ciencias Biológicas y de la Salud, Universidad Autónoma Metropolitana-Xochimilco (UAM-X), Ciudad de México 04960, Mexico*

Martha Lydia Macías-Rubalcava − *Instituto de Química, Universidad Nacional Autónoma de México, Ciudad de México 04510, Mexico;* orcid.org/0000-0001-9650-0920

Huzefa A. Raja − *Department of Chemistry and Biochemistry, University of North Carolina at Greensboro, Greensboro, North Carolina 27412, United States;* orcid.org/0000-0002-0824-9463

Martín González-Andrade − *Facultad de Medicina, Universidad Nacional Autónoma de México, Ciudad de México 04510, Mexico*

Complete contact information is available at: https://pubs.acs.org/10.1021/acsomega.1c03708

Author Contributions

This work was taken for the Ph.D. Thesis of D.R.-R. submitted to Posgrado en Ciencias Químicas, UNAM.

Notes

The authors declare no competing financial interest.

ACKNOWLEDGMENTS

This work was supported by grants from CONACyT CB A1-S-11226 and DGAPA IN 217320 awarded to R.M. D.R.-R. (768720) acknowledges the fellowship from CONACyT to pursue graduate studies. The authors are deeply grateful to Dr. Juventino García-Alejandre and Diego A. Roa, for providing the means to pursue the reduction of compound **1**. The authors also acknowledge the support of Drs. Esperanza Carcache de Blanco and Gerardo D. Anaya-Eugenio from the College of Pharmacy, The Ohio State University, United States for their valuable support for recording the ^{1}H and ^{13}C NMR, and ECD spectra of compound **1a**/**1b**, as well as its optical rotation. The authors also recognize the valuable support of I. Rivero and A. Pérez-Vásquez from Facultad de Química. The authors are grateful to Dr. Beatriz Quiroz García, Dr. Ma. del Carmen García-González, and MSc. Simón Hernández-Ortega from Instituto de Química for recording some of the NMR spectra, MS spectra, and for X-ray analysis of compound **9**, respectively. The authors are indebted to Dirección General de Cómputo y de Tecnologías de Información y Comunicación (DGTIC), UNAM, for the resources to carry out computational calculations through the Miztli supercomputing system (LANCAD-UNAM-DGTIC-313).

REFERENCES

(1) International Diabetes Federation. *IDF Diabetes Atlas*, 9th ed.; International Diabetes Federation: Brussels, Belgium, 2019.

(2) Upadhyay, J.; Polyzos, S. A.; Perakakis, N.; Thakkar, B.; Paschou, S. A.; Katsiki, N.; Underwood, P.; Park, K.-H.; Seufert, J.; Kang, E. S.; Sternthal, E.; Karagiannis, A.; Mantzoros, C. S. Pharmacotherapy of type 2 diabetes: An update. *Metabolism* **2018**, *78*, 13−42.

(3) Kerru, N.; Singh-Pillay, A.; Awolade, P.; Singh, P. Current anti-diabetic agents and their molecular targets: A review. *Eur. J. Med. Chem.* **2018**, *152*, 436−488.

(4) Chan, C.-W.; Yu, C.-L.; Lin, J.-C.; Hsieh, Y.-C.; Lin, C.-C.; Hung, C.-Y.; Li, C. H.; Liao, Y.-C.; Lo, C.-P.; Huang, J.-L.; Lin, C.-H.; Wu, T.-J. Glitazones and alpha-glucosidase inhibitors as the second-line oral anti-diabetic agents added to metformin reduce cardiovascular risk in Type 2 diabetes patients: a nationwide cohort observational study. *Cardiovasc. Diabetol.* **2018**, *17*, No. 20.

(5) Verastegui-Omaña, B.; Rebollar-Ramos, D.; Pérez-Vásquez, A.; Martínez, A. L.; Madariaga-Mazón, A.; Flores-Bocanegra, L.; Mata, R. α-Glucosidase inhibitors from *Malbranchea flavorosea*. *J. Nat. Prod.* **2017**, *80*, 190−195.

(6) Rebollar-Ramos, D.; Macías-Ruvalcaba, M. L.; Figueroa, M.; Raja, H. A.; González-Andrade, M.; Mata, R. Additional α-Glucosidase inhibitors from *Malbranchea flavorosea* (Leotiomycetes, Ascomycota). *J. Antibiot.* **2018**, *71*, 862−871.

(7) Rangel-Grimaldo, M.; Macías-Rubalcava, M. L.; González-Andrade, M.; Raja, H. A.; Figueroa, M.; Mata, R. α-Glucosidase and protein tyrosine phosphatase 1B inhibitors from *Malbranchea circinata*. *J. Nat. Prod.* **2020**, *83*, 675−683.

(8) Díaz-Rojas, M.; Raja, H. A.; González-Andrade, M.; Rivera-Chávez, J.; Rangel-Grimaldo, M.; Rivero-Cruz, I.; Mata, R. Protein tyrosine phosphatase 1B inhibitors from the fungus *Malbranchea albolutea*. *Phytochemistry* **2021**, *184*, No. 112664.

(9) Sigler, L.; Carmichael, J. W. Taxonomy of *Malbranchea* and some other Hyphomycetes with arthroconidia. *Mycotaxon* **1976**, *4*, 349−488.

(10) Martínez-Luis, S.; Rodríguez, R.; Acevedo, L.; González, M. C.; Lira-Rocha, A.; Mata, R. Malbrancheamide, a new calmodulin inhibitor from the fungus *Malbranchea aurantiaca*. *Tetrahedron* **2006**, *62*, 1817−1822.

(11) Figueroa, M.; González, M. C.; Mata, R. Malbrancheamide B, a novel compound from the fungus *Malbranchea aurantiaca*. *Nat. Prod. Res.* **2008**, *22*, 709−714.

(12) Watts, K. R.; Loveridge, S. T.; Tenney, K.; Media, J.; Valeriote, F. A.; Crews, P. Utilizing DART mass spectrometry to pinpoint halogenated metabolites from a marine invertebrate-derived fungus. *J. Org. Chem.* **2011**, *76*, 6201−6208.

(13) Madariaga-Mazón, A.; Hernández-Abreu, O.; Estrada-Soto, S.; Mata, R. insights on the vasorelaxant mode of action of malbrancheamide. *J. Pharm. Pharmacol.* **2015**, *67*, 551−558.

(14) Martínez-Luis, S.; González, M. C.; Ulloa, M.; Mata, R. Phytotoxins from the fungus *Malbranchea aurantiaca*. *Phytochemistry* **2005**, *66*, 1012−1016.

(15) Wakana, D.; Hosoe, T.; Wachi, H.; Itabashi, T.; Fukushima, K.; Yaguchi, T.; Kawai, K.-I. The cytotoxic and antifungal activities of two new sesquiterpenes, malfilanol A and B, derived from *Malbranchea filamentosa*. *J. Antibiot.* **2009**, *62*, 217−219.

(16) Schlegel, B.; Hanel, F.; Gollmick, F. A.; Saluz, H.-P.; Gräfe, U. New quinones and hydroquinones from *Malbranchea cinnamomea* HKI 286 and HKI 296 and interaction with Tax/CREB expression system in yeast. *J. Antibiot.* **2003**, *56*, 917−922.

(17) Schlegel, B.; Härtl, A.; Gollmick, F. A.; Gräfe, U. 7-Methoxy-2,3-dimethylbenzofuran-5-ol, a new antioxidant from *Malbranchea cinnamomea* HKI 0286. *J. Antibiot.* **2003**, *56*, 792−794.

(18) Wakana, D.; Hosoe, T.; Itabashi, T.; Okada, H.; Fukushima, K.; Kawai, K.-I. Structures of new triterpene glycosides, malbrancheosides A-D, from *Malbranchea filamentosa*. *Heterocycles* **2008**, *75*, 1109−1122.

(19) Wakana, D.; Itabashi, T.; Kawai, K.-I.; Yaguchi, T.; Fukushima, K.; Goda, Y.; Hosoe, T. Cytotoxic anthrasteroid glycosides,

malsterosides A-C, from *Malbranchea filamentosa*. *J. Antibiot.* **2014**, *67*, 585−588.
(20) Hosoe, T.; Iizuka, T.; Komai, S.-I.; Wakana, D.; Itabashi, T.; Nozawa, K.; Fukushima, K.; Kawai, K.-I. 4-Benzyl-3-phenyl-5H-furan-2-one, a vasodilator isolated from *Malbranchea filamentosa* IFM 41300. *Phytochemistry* **2005**, *66*, 2776−2779.
(21) Wakana, D.; Hosoe, T.; Itabashi, T.; Fukushima, K.; Kawai, K.-I. 2008. Two new furanone glycosides, malfilamentosides A and B, from *Malbranchea filamentosa*. *Mycotoxins* **2008**, *58*, 1−6.
(22) Yang, Y.-L.; Liao, W.-Y.; Liu, W.-Y.; Liaw, C.-C.; Shen, C.-N.; Huang, Z.-Y.; Wu, S.-H. Discovery of new natural products by intact-cell mass spectrometry and LC-SPE-NMR: malbranpyrroles, novel polyketides from thermophilic fungus *Malbranchea sulfurea*. *Chem. − Eur. J.* **2009**, *15*, 11573−11580.
(23) White, T. J.; Bruns, T.; Lee, S. H.; Taylor, J. W. *PCR Protocols: A Guide to Methods and Application*; Elsevier: San Diego, 1990; pp 315−322.
(24) Gardes, M.; Bruns, T. D. ITS primers with enhanced specificity for basidiomycetes − application to the identification of mycorrhizae and rusts. *Mol. Ecol.* **1993**, *2*, 113−118.
(25) Clark, B.; Capon, R. J.; Lacey, E.; Tennant, S.; Gill, J. H.; Bulheller, B.; Bringmann, G. Gymnoascolides A-C: aromatic butenolides from an Australian isolate of the soil ascomycete *Gymnoascus reessii*. *J. Nat. Prod.* **2005**, *68*, 1226−1230.
(26) Hamasaki, T.; Sato, Y.; Hatsuda, Y. Structure of sydowinin A, sydowinin B, and sydowinol, metabolites from *Aspergillus sydowi*. *Agric. Biol. Chem.* **1975**, *39*, 2341−2345.
(27) Kim, H. S.; Park, I. Y.; Park, Y. J.; Lee, J. H.; Hong, Y. S.; Lee, J. J. A novel dihydroxanthenone, AGI-B4 with inhibition of VEGF-induced endothelial cell growth. *J. Antibiot.* **2002**, *55*, 669−672.
(28) Bunbamrung, N.; Intaraudom, C.; Supothina, S.; Komwijit, S.; Pittayakhajonwut, P. Antibacterial and anti-phytopathogenic substances from the insect pathogenic fungus *Gibellula* sp. BCC36964. *Phytochem. Lett.* **2015**, *12*, 142−147.
(29) Wang, W.; Gao, M.; Luo, Z.; Liao, Y.; Zhang, B.; Ke, W.; Shao, Z.; Li, F.; Chen, J. Secondary metabolites isolated from the deep sea-derived fungus *Aspergillus sydowii* C1-S01-A7. *Nat. Prod. Res.* **2019**, *33*, 3077−3082.
(30) Yao, Q.; Wang, J.; Zhang, X.; Nong, X.; Xu, X.; Qi, S. Cytotoxic polyketides from the deep-sea-derived fungus *Engyodontium album* DFFSCS021. *Mar. Drugs* **2014**, *12*, 5902−5915.
(31) Tan, Q.-W.; Ouyang, M.-A.; Shen, S.; Li, W. Bioactive metabolites from a marine-derived strain of the fungus *Neosartorya fischeri*. *Nat. Prod. Res.* **2012**, *26*, 1402−1407.
(32) Bao, J.; He, F.; Yu, J. H.; Zhai, H.; Cheng, Z. Q.; Jiang, C. S.; Zhang, Y.; Zhang, Y.; Zhang, X.; Chen, G.; Zhang, H. New chromones from a marine-derived fungus, *Arthrinium* sp., and their biological activity. *Molecules* **2018**, *23*, No. 1982.
(33) Tang, X. X.; Liu, S. Z.; Sun, Y. Y.; He, F. M.; Xu, G. X.; Fang, M. J.; Zhen, W.; Qiu, Y. K. New cyclopentenoneacrylic acid derivatives from a marine-derived fungus *Trichoderma atroviride* H548. *Nat. Prod. Res.* **2020**, *11*, 1−8.
(34) Ma, L.-Y.; Zhang, H.-B.; Kang, H.-H.; Zhong, M.-J.; Liu, D.-S.; Ren, H.; Liu, W. Z. New butenolides and cyclopentenones from saline soil-derived fungus *Aspergillus sclerotiorum*. *Molecules* **2019**, *24*, No. 2642.
(35) Engelking, L. R. Chapter 6 − Enzyme Kinetics. In *Textbook of Veterinary Physiological Chemistry*, 3rd ed.; Engelking, L. R., Ed.; Academic Press: San Diego, 2015; pp 32−38.
(36) Muller, G. Chapter K: Antidiabetic Activity. In *Drug Discovery and Evaluation: Pharmacological Assays*, 3rd ed.; Vogel, H. G., Ed.; Springer: New York, 2008; pp 1327−1607.
(37) Benedé-Ubieto, R.; Estévez-Vázquez, O.; Ramadori, P.; Cubero, F. J.; Nevzorova, Y. A. Guidelines and considerations for metabolic tolerance tests in mice. *Diabetes Metab. Syndr. Obes.* **2020**, *13*, 439−450.
(38) Daina, A.; Michielin, O.; Zoete, V. SwissADME: a free web tool to evaluate pharmacokinetics, drug-likeness and medicinal chemistry friendliness of small molecules. *Sci. Rep.* **2017**, *7*, No. 42717.
(39) Sander, T. OSIRIS Property Explorer. https://www.organic-chemistry.org/prog/peo/ (accessed June 20, 2021).
(40) Baell, J. B.; Holloway, G. A. New substructure filters for removal of pan assay interference compounds (PAINS) from screening libraries and for their exclusion in bioassays. *J. Med. Chem.* **2010**, *53*, 2719−2740.
(41) Brenk, R.; Schipani, A.; James, D.; Krasowski, A.; Gilbert, I. H.; Frearson, J.; Wyatt, P. G. Lessons learnt from assembling screening libraries for drug discovery for neglected diseases. *ChemMedChem* **2008**, *3*, 435−444.
(42) Teague, S. J.; Davis, A. M.; Leeson, P. D.; Oprea, T. The design of leadlike combinatorial libraries. *Angew. Chem., Int. Ed.* **1999**, *38*, 3743−3748.
(43) Lipinski, C. A.; Lombardo, F.; Dominy, B. W.; Feeney, P. J. Experimental and computational approaches to estimate solubility and permeability in drug discovery and development settings. *Adv. Drug Delivery Rev.* **2012**, *64*, 4−17.
(44) Egan, W. J.; Merz, K. M.; Baldwin, J. J. Prediction of drug absorption using multivariate statistics. *J. Med. Chem.* **2000**, *43*, 3867−3877.
(45) Veber, D. F.; Johnson, S. R.; Cheng, H.-Y.; Smith, B. R.; Ward, K. W.; Kopple, K. D. Molecular properties that influence the oral bioavailability of drug candidates. *J. Med. Chem.* **2002**, *45*, 2615−2623.
(46) Muegge, I.; Heald, S. L.; Brittelli, D. Simple selection criteria for drug-like chemical matter. *J. Med. Chem.* **2001**, *44*, 1841−1846.
(47) Ghose, A. K.; Viswanadhan, V. N.; Wendoloski, J. J. A knowledge-based approach in designing combinatorial or medicinal chemistry libraries for drug discovery. 1. A qualitative and quantitative characterization of known drug databases. *J. Comb. Chem.* **1999**, *1*, 55−68.
(48) Ur Rehman, N.; Halim, S. A.; Al-Azri, M.; Khan, M.; Khan, A.; Rafiq, K.; Al-Rawahi, A.; Csuk, R.; Al-Harrasi, A. Triterpenic acids as non-competitive α-glucosidase inhibitors from *Boswellia elongata* with structure-activity relationship: in vitro and *in silico* studies. *Biomolecules* **2020**, *10*, No. 751.
(49) Li, S.; Zhang, J.; Lu, S.; Huang, W.; Geng, L.; Shen, Q.; Zhang, J. The mechanism of allosteric inhibition of protein tyrosine phosphatase 1B. *PLoS One* **2014**, *9*, No. e97668.
(50) Wiesmann, C.; Barr, K. J.; Kung, J.; Zhu, J.; Erlanson, D. A.; Shen, W.; Fahr, B. J.; Zhong, M.; Taylor, L.; Randal, M.; McDowell, R. S.; Hansen, S. K. allosteric inhibition of protein tyrosine phosphatase 1B. *Nat. Struct. Mol. Biol.* **2004**, *11*, 730−737.
(51) Raja, H. A.; Miller, A. N.; Pearce, C. J.; Oberlies, N. H. Fungal identification using molecular tools: a primer for the natural products research community. *J. Nat. Prod.* **2017**, *80*, 756−770.
(52) Schoch, C. L.; Robbertse, B.; Robert, V.; Vu, D.; Cardinali, G.; Irinyi, L.; Meyer, W.; Nilsson, R. H.; Hughes, K.; Miller, A. N.; Kirk, P. M.; Abarenkov, K.; Aime, M. C.; Ariyawansa, H. A.; Bidartondo, M.; Boekhout, T.; Buyck, B.; Cai, Q.; Chen, J.; Crespo, A.; Crous, P. W.; Damm, U.; De Beer, Z. W.; Dentinger, B. T.; Divakar, P. K.; Duenas, M.; Feau, N.; Fliegerova, K.; Garcia, M. A.; Ge, Z. W.; Griffith, G. W.; Groenewald, J. Z.; Groenewald, M.; Grube, M.; Gryzenhout, M.; Gueidan, C.; Guo, L.; Hambleton, S.; Hamelin, R.; Hansen, K.; Hofstetter, V.; Hong, S. B.; Houbraken, J.; Hyde, K. D.; Inderbitzin, P.; Johnston, P. R.; Karunarathna, S. C.; Koljalg, U.; Kovacs, G. M.; Kraichak, E.; Krizsan, K.; Kurtzman, C. P.; Larsson, K. H.; Leavitt, S.; Letcher, P. M.; Liimatainen, K.; Liu, J. K.; Lodge, D. J.; Luangsa-ard, J. J.; Lumbsch, H. T.; Maharachchikumbura, S. S.; Manamgoda, D.; Martin, M. P.; Minnis, A. M.; Moncalvo, J. M.; Mule, G.; Nakasone, K. K.; Niskanen, T.; Olariaga, I.; Papp, T.; Petkovits, T.; Pino-Bodas, R.; Powell, M. J.; Raja, H. A.; Redecker, D.; Sarmiento-Ramirez, J. M.; Seifert, K. A.; Shrestha, B.; Stenroos, S.; Stielow, B.; Suh, S. O.; Tanaka, K.; Tedersoo, L.; Telleria, M. T.; Udayanga, D.; Untereiner, W. A.; Dieguez Uribeondo, J.; Subbarao, K. V.; Vagvolgyi, C.; Visagie, C.; Voigt, K.; Walker, D. M.; Weir, B. S.; Weiss, M.; Wijayawardene, N. N.; Wingfield, M. J.; Xu, J. P.; Yang, Z. L.; Zhang, N.; Zhuang, W. Y.; Federhen, S. Finding needles in

https://doi.org/10.1021/acsomega.1c03708
ACS Omega 2021, 6, 22969−22981

haystacks: linking scientific names, reference specimens and molecular data for fungi. *Database* **2014**, *2014*, No. bau061.
(53) Sigler, L.; Hambleton, S.; Flis, A. L.; Pare, J. A. Auxarthron teleomorphs for *Malbranchea filamentosa* and *Malbranchea albolutea* and relationships within Auxarthron. *Stud. Mycol.* **2002**, *47*, 111−122.
(54) Sarrocco, S.; Diquattro, S.; Baroncelli, R.; Cimmino, A.; Evidente, A.; Vannacci, G.; Doveri, F. A polyphasic contribution to the knowledge of Auxarthron (Onygenaceae). *Mycol. Prog.* **2015**, *14*, No. 112.
(55) Hubka, V.; Dobiasova, S.; Lyskova, P.; Mallatova, N.; Chlebkova, J.; Skorepova, M.; Kubatova, A.; Dobias, R.; Chudickova, M.; Kolarik, M. *Auxarthron ostraviense* sp. nov., and *A. umbrinum* associated with non-dermatophytic onychomycosis. *Med. Mycol.* **2013**, *51*, 614−624.
(56) Kalyaanamoorthy, S.; Minh, B. Q.; Wong, T. K.; von Haeseler, A.; Jermiin, L. S. ModelFinder: fast model selection for accurate phylogenetic estimates. *Nat. Methods* **2017**, *14*, 587−589.
(57) Posada, D.; Buckley, T. R. Model selection and model averaging in phylogenetics: Advantages of akaike information criterion and bayesian approaches over likelihood ratio tests. *Syst. Biol.* **2004**, *53*, 793−808.
(58) Talavera, G.; Castresana, J. Improvement of phylogenies after removing divergent and ambiguously aligned blocks from protein sequence alignments. *Syst. Biol.* **2007**, *56*, 564−577.
(59) Castresana, J. Selection of conserved blocks from multiple alignments for their use in phylogenetic analysis. *Mol. Biol. Evol.* **2000**, *17*, 540−552.
(60) Zhang, D.; Gao, F.; Jakovlić, I.; Zou, H.; Zhang, J.; Li, W. X.; Wang, G. T. PhyloSuite: An integrated and scalable desktop platform for streamlined molecular sequence data management and evolutionary phylogenetics studies. *Mol. Ecol. Resour.* **2020**, *20*, 348−355.
(61) Minh, B. Q.; Nguyen, M. A. T.; von Haeseler, A. Ultrafast approximation for phylogenetic bootstrap. *Mol. Biol. Evol.* **2013**, *30*, 1188−1195.
(62) Nguyen, L.-T.; Schmidt, H. A.; von Haeseler, A.; Minh, B. Q. IQ-TREE: A fast and effective stochastic algorithm for estimating maximum-likelihood phylogenies. *Mol. Biol. Evol.* **2015**, *32*, 268−274.
(63) Deangelis, A.; Dmitrenko, O.; Fox, J. M. Rh-Catalyzed intermolecular reactions of cyclic α-diazocarbonyl compounds with selectivity over tertiary C-H bond migration. *J. Am. Chem. Soc.* **2012**, *134*, 11035−11043.
(64) Copeland, R. A. *Enzymes: A Practical Introduction to Structure, Mechanism, and Data Analysis*, 2nd ed.; Wiley-VCH: New York, 2001; pp 1−397.
(65) Bruhn, T.; Schaumlöffel, A.; Hemberger, Y.; Pescitelli, G. *SpecDis*, version 1.71; JIMDO: Berlin, Germany, http://specdis-software.jimdo.com, 2017.
(66) Salentin, S.; Schreiber, S.; Haupt, V. J.; Adasme, M. F.; Schroeder, M. PLIP: Fully automated protein-ligand interaction profiler. *Nucleic Acids Res.* **2015**, *43*, W443−W447.
(67) Case, D. A.; Cheatham, T. E.; Darden, T.; Gohlke, H.; Luo, R.; Merz, K. M.; Onufriev, A.; Simmerling, C.; Wang, B.; Woods, R. J. The Amber biomolecular simulation programs. *J. Comput. Chem.* **2005**, *26*, 1668−1688.
(68) Case, D. A.; Darden, T.; Cheatham, T. E.; Simmerling, C.; Wang, J.; Duke, R. E.; Luo, R.; Walker, R. C.; Zhang, W.; Merz, K. M.; Roberts, B. P.; Hayik, S.; Roitberg, A.; Seabra, G.; Swails, J.; Götz, A. W.; Kolossváry, I.; Wong, K. F.; Paesani, F.; Kollman, P. *Amber 12*; University of California: San Francisco, 2012.
(69) Walker, R. C.; Crowley, M. F.; Case, D. A. The implementation of a fast and accurate QM/MM potential method in Amber. *J. Comput. Chem.* **2008**, *29*, 1019−1031.
(70) Tian, C.; Kasavajhala, K.; Belfon, K. A. A.; Raguette, L.; Huang, H.; Migues, A. N.; Bickel, J.; Wang, Y.; Pincay, J.; Wu, Q.; Simmerling, C. ff19SB: Amino-acid-specific protein backbone parameters trained against quantum mechanics energy surfaces in solution. *J. Chem. Theory Comput.* **2020**, *16*, 528−552.
(71) Salomon-Ferrer, R.; Götz, A. W.; Poole, D.; Le Grand, S.; Walker, R. C. Routine microsecond molecular dynamics simulations with AMBER on GPUs. 2. Explicit solvent particle mesh ewald. *J. Chem. Theory Comput.* **2013**, *9*, 3878−3888.
(72) Roe, D. R.; Cheatham, T. E. PTRAJ and CPPTRAJ: software for processing and analysis of molecular dynamics trajectory data. *J. Chem. Theory Comput.* **2013**, *9*, 3084−3095.

https://doi.org/10.1021/acsomega.1c03708
ACS Omega 2021, 6, 22969−22981